Mountain-Wave Momentum Flux in an Evolving Synoptic-Scale Flow

CHIH-CHIEH CHEN, DALE R. DURRAN, AND GREGORY J. HAKIM

Department of Atmospheric Sciences, University of Washington, Seattle, Washington

(Manuscript received 24 September 2004, in final form 25 February 2005)

ABSTRACT

The evolution of mountain-wave-induced momentum flux is examined through idealized numerical simulations during the passage of a time-evolving synoptic-scale flow over an isolated 3D mountain of height h. The dynamically consistent synoptic-scale flow U accelerates and decelerates with a period of 50 h; the maximum wind arrives over the mountain at 25 h. The synoptic-scale static stability N is constant, so the time dependence of the nonlinearity parameter, $\varepsilon(t) = Nh/U(t)$, is symmetric about a minimum value at 25 h.

The evolution of the vertical profile of momentum flux shows substantial asymmetry about the midpoint of the cycle even though the nonlinearity parameter is symmetric. Larger downward momentum fluxes are found during the accelerating phase, and the largest momentum fluxes occur in the mid- and upper troposphere before the maximum background flow arrives at the mountain. For a period of roughly 15 h, this vertical distribution of momentum flux accelerates the lower-tropospheric zonal-mean winds due to low-level momentum flux convergence.

Conservation of wave action and Wentzel–Kramers–Brillouin (WKB) ray tracing are used to reconstruct the time–altitude dependence of the mountain-wave momentum flux in a semianalytic procedure that is completely independent of the full numerical simulations. For quasi-linear cases, the reconstructions show good agreement with the numerical simulations, implying that the basic asymmetry obtained in the full numerical simulations may be interpreted using WKB theory. These results demonstrate that even slow variations in the mean flow, with a time scale of 2 days, play a dominant role in regulating the vertical profile of mountain-wave-induced momentum flux.

The time evolution of cross-mountain pressure drag is also examined in this study. For almost-linear cases, the pressure drag is well predicted under steady-state linear theory by using the instantaneous incident flow. Nevertheless, for mountains high enough to preserve a moderate degree of nonlinearity when the synoptic-scale incident flow is strongest, the evolution of cross-mountain pressure drag is no longer symmetric about the time of maximum wind. A higher drag state is found when the cross-mountain flow is accelerating. These results suggest that the local character of the topographically induced disturbance cannot be solely determined by the instantaneous value of the nonlinearity parameter ε.

1. Introduction

Stably stratified airflow over mountains produces gravity waves that transport momentum vertically (Sawyer 1959; Eliassen and Palm 1960; Bretherton 1969). The vertical divergence of mountain-wave-induced momentum fluxes has been shown to produce an important drag on the large-scale atmospheric flow (Lilly 1972; Palmer et al. 1986; McFarlane 1987), and is now parameterized in most large-scale models of the atmospheric circulation. The estimates of orographic gravity wave drag currently used in these parameterizations rely on steady-state descriptions of the mountain-wave response [see Table 1 in Kim and Arakawa (1995) for an overview]. Indeed, even most theoretical investigations of mountain waves, whether numerical or analytic have focused on the response to steady upstream forcing either through direct solution of the steady-state governing equations or as the solution to an initial value problem in a steady large-scale flow [Smith (1979) and Durran (1986) provide reviews].

The mountain-wave problem that has received the most theoretical attention is one in which the large-scale cross-mountain wind speed U and static stability N are constant. This paper extends this canonical problem to include mean flows that change very slowly with time and horizontal position. As will be demonstrated,

Corresponding author address: Chih-Chieh Chen, Dept. of Atmospheric Sciences, University of Washington, Box 351640, Seattle, WA 98195-1640.
E-mail: cchen@atmos.washington.edu

© 2005 American Meteorological Society

the magnitude and vertical profiles of mountain-wave-induced momentum flux in such flows can be very different from those that would be predicted from steady-state theory using the instantaneous value of the large-scale wind speed over the mountain crest.

Among those who have investigated mountain waves in a nonsteady environment, both Crook et al. (1990) and Nance and Durran (1997) studied the wave response to an imposed transition in the background flow between two steady states. Bell (1975) and Bannon and Zehnder (1985) obtained solutions to the linearized two-dimensional governing equations for a periodically varying mean flow. Their solutions neglect any initial transients, effectively assuming that the flow has had an infinite amount of time to adjust to the steady periodic forcing. This is a situation that may be more appropriate for tidally forced flows in the ocean than episodic development of mountain waves in the atmosphere. Bannon and Zehnder give a careful discussion of the time-varying pressure drag on the topography, but do not discuss the vertical distribution of the associated mountain-wave momentum flux. Lott and Teitelbaum (1993a,b) compute solutions to the linearized two-dimensional governing equations for mountain waves in a time-varying mean flow that accelerates from an initial state of rest. They investigate the dependence of the wave amplitude and momentum flux profile as a function of γ, the ratio of the time scale for variations in the large-scale forcing to the advective time scale for the cross-mountain flow [defined in (5)].

This paper extends the investigations of Lott and Teitelbaum (1993a,b) by using a nonlinear numerical model to compute solutions to an initial value problem in which a stagnant air mass over an isolated ridge begins to accelerate in a dynamically consistent three-dimensional synoptic-scale flow. Both small and finite-amplitude ridges are considered. The use of a dynamically consistent synoptic-scale flow ensures that all large-scale flow deceleration or acceleration is accompanied by appropriate fields of horizontal confluence or difluence, which turns out to have a nontrivial impact on the mountain-wave intensity. In the spirit of the canonical constant-N and -U mountain-wave problem, our idealized cross-mountain flow includes only the most basic representation of the variations in the horizontal wind field that must accompany the passage of a localized barotropic jet over a mountain ridge.

We focus on problems for which the large-scale flow over the mountain increases from 0 to 20 m s^{-1} and then returns to 0 over a meteorologically relevant period of approximately 2 days. The temporal variation jof the resulting waves is similar to that in the most slowly evolving (quasi-steady) case examined by Lott and Teitelbaum (1993a,b), but the γ for our simulations is approximately 5 times larger than the γ for their quasi-steady case. Lott and Teitelbaum suggested that when $\gamma \gg 1$, "roughly the momentum flux remains that predicted by the stationary theory"; yet even though $\gamma = 100$ in our simulations, we find major differences between the momentum fluxes in the slowly varying flow and those predicted from steady-state theory.

2. Model equations and experimental design

The mathematics describing the waves and the large-scale flow are simplified using the Boussinesq and f-plane approximations. To avoid the numerical complications associated with solving a Poisson equation for pressure in terrain-following coordinates, we retain a prognostic equation for the pressure and solve the compressible Boussinesq system using the nonlinear numerical model previously employed by Epifanio and Durran (2001).[1] The governing equations are

$$\frac{D\mathbf{v}}{Dt} + f\mathbf{k} \times \mathbf{v} + \nabla P = g\left(\frac{\theta - \theta_r}{\theta_0}\right)\mathbf{k} - \nabla \cdot \mathbf{T}, \quad (1)$$

$$\frac{D\theta}{Dt} = \nabla \cdot \mathbf{H}, \quad (2)$$

$$\frac{\partial P}{\partial t} + u_0 \frac{\partial P}{\partial x} + c_{s_0}^2 \nabla \cdot \mathbf{v} = 0, \quad (3)$$

where

$$\frac{D}{Dt} = \frac{\partial}{\partial t} + (u_0 + u)\frac{\partial}{\partial x} + \upsilon \frac{\partial}{\partial y} + w \frac{\partial}{\partial z}.$$

Here (x, y, z) is the spatial position vector, $\mathbf{k}$ is the vertical unit vector, and f is the Coriolis parameter. Symbols with subscript 0 denote constant reference values; u_0 is a constant westerly flow in geostrophic balance with a vertically uniform north–south pressure distribution $-fu_0y$; P is the Boussinesq pressure perturbation about $-fu_0y$, and $\mathbf{v} = (u, \upsilon, w)$ is the perturbation velocity vector with respect to $(u_0, 0, 0)$. The potential temperature is θ; c_{s_0} is the speed of sound; and g is gravity. Let c_p be the specific heat of air at constant pressure and R the gas constant. Define the Exner func-

[1] Signal propagation at the speed of sound dominates that due to advection in (3) so that the first two terms could be replaced by DP/Dt without changing the numerical solution in even the most nonlinear case considered in this paper. Alternatively, if the $u_0\partial P/\partial x$ term in (3) is simply dropped, there are minor quantitative but no qualitative differences in the solution. The particular form chosen for the advective operator in (3) allows the specification of a simple exact solution when no mountain is present.

tion as $\pi = (p/p_0)^{R/c_p}$, and divide π and θ into a vertically varying reference state and a remainder such that $\pi = \pi_r(z) + \pi_g(y) + \pi'(x, y, z, t)$ and $\theta = \theta_r(z) + \theta'(x, y, z, t)$, where the reference state (π_r, θ_r) is in hydrostatic balance ($c_p\theta_r\partial\pi_r/\partial z = -g$), and π_g is a barotropic pressure perturbation balancing the mean flow ($c_p\theta_0\partial\pi_g/\partial y = -fu_0$). Then the perturbation Boussinesq pressure may be defined in an atmospheric context as $P = c_p\theta_0\pi'$ (see Durran 1999, p. 24). In these simulations $\theta_0 = 288$ K.

Finally, **T** and **H** are the turbulent subgrid-scale fluxes of momentum and heat, parameterized in terms of an eddy diffusivity K following Lilly (1962); they may be expressed in tensor notation as

$$T_{ij} = KD_{ij}, \quad H_j = K\frac{\partial\theta}{\partial x_j}.$$

Here the Prandtl number has been taken as unity,

$$D_{ij} = \frac{\partial u_i}{\partial x_j} + \frac{\partial u_j}{\partial x_i} - \delta_{ij}\frac{2}{3}\frac{\partial u_\ell}{\partial x_\ell},$$

$(x_1, x_2, x_3) = (x, y, z)$, $(u_1, u_2, u_3) = (u, v, w)$, and K is proportional to $(1 - \mathrm{Ri})^{1/2}$, in which Ri is the Richardson number

$$\mathrm{Ri} = \frac{2g}{\theta}\frac{\partial\theta}{\partial x_3}\left(\sum_i\sum_j D_{ij}^2\right)^{-1}.$$

The numerical approximation of (1)–(3) follows the formulation in Durran and Klemp (1983) except that the buoyancy force and the potential temperature tendency due to vertical motion acting on the mean stratification are included as part of the implicit differencing on the small time step.

The initial condition is a dynamically consistent synoptic-scale disturbance consisting of the superposition of a uniform westerly mean flow at speed u_0 and a barotropic square wave with horizontal velocities (u_s, v_s), amplitude u_0, and wavelength L given by

$$u_s(x, y, z) = u_0\cos\left[\frac{2\pi(x - x_0)}{L}\right]\cos\left(\frac{2\pi y}{L}\right)$$

$$v_s(x, y, z) = u_0\sin\left[\frac{2\pi(x - x_0)}{L}\right]\sin\left(\frac{2\pi y}{L}\right).$$

The initial potential temperature field is uniform in the horizontal and increases with height such that $N = 0.01$ s^{-1}. The initial perturbation pressure P_s is in steady-state nonlinear balance with respect to the square-wave horizontal velocities such that

$$\nabla\cdot[(\mathbf{v}_\mathbf{s}\cdot\nabla)\mathbf{v}_\mathbf{s} + f\mathbf{k}\times\mathbf{v}_\mathbf{s}] + \nabla^2 P_s = 0, \tag{4}$$

where $\mathbf{v}_\mathbf{s} = (u_s, v_s)$. In contrast to the symmetry in the velocity perturbations in the square wave, the nonlinear balance yields an asymmetric pressure field with stronger lows and weaker highs. In the absence of topography, the square wave is an exact solution to the nonlinear governing Eqs. (1)–(3) that translates eastward without changing form in the mean flow at speed u_0, that is, the large-scale flow is given by

$$U = u_s(x - u_0t, y, t) + u_0, \quad V = v_s(x - u_0t, y, t),$$

$$W = 0, \quad P_{Ls} = P_s(x - u_0t, y, t).$$

Unless otherwise specified, $u_0 = 10$ m s^{-1} and $L = 1800$ km, implying that all synoptic-scale fields are periodic with a period τ of 50 h.

The mountain is taken to be a uniform ridge of finite length centered in the region of initially stagnant flow at $(x, y) = (x_0, L/2)$. As in Epifanio and Durran (2001), it is given by

$$h_s(x, y) = \begin{cases} \dfrac{h}{16}\left[1 + \cos\left(\dfrac{\pi r}{4a}\right)\right]^4, & \text{if} \quad r \le 4a; \\ 0, & \text{otherwise,} \end{cases}$$

where

$$r^2 = \begin{cases} (x - x_0)^2 + (|y - L/2| - (\beta - 1)a)^2, & \text{if} \quad |y - L/2| > (\beta - 1)a; \\ (x - x_0)^2, & \text{otherwise.} \end{cases}$$

In these simulations the approximate half-width at half-height a is 18 km, the aspect ratio β is 5, $x_0 = 225$ km, the height of the ridge h is varied between 125 and 1000 m in these simulations.

Initial distributions of $P - fu_0y$ and $u + u_0$ are shown in Fig. 1. The computational domain is doubly periodic over a distance of $L = 1800$ km in both x and y, with a horizontal grid spacing of 6 km. The physically relevant portion of the computational domain is 16 km deep; this is topped by a 16-km-deep wave-absorbing layer. A stretched grid is employed in the vertical with $\Delta z = 150$ m for $z < 10$ km, above which Δz gradually increases to 500 m over the interval $10 < z < 15$ km and remains a constant 500 m for $z > 15$ km. The size of the large and

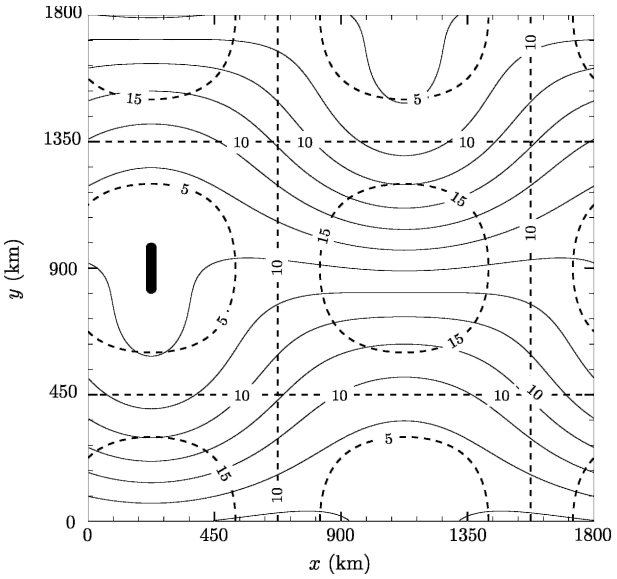

FIG. 1. Isobars of π' (thin lines, contour interval 5×10^{-4}) and zonal wind speed (thick dashed lines, contour interval 5 m s^{-1}) of the initial synoptic-scale flow. The mountain ridge (black shading) is centered at $(x, y) = (225, 900)$ km.

small time steps is varied depending on the strength of the mountain-wave response; they are 100 and 10 s, respectively, for the 250-m mountain.

The lower boundary condition is free-slip along the topography,

$$w(x, y, h_s) = (u + u_0)\frac{\partial h_s}{\partial x} + v\frac{\partial h_s}{\partial y}.$$

A rigid lid is the appropriate upper boundary condition for the barotropic large-scale flow, but the rigid lid is not suitable for mountain waves, which must transport energy vertically through the upper boundary without creating spurious reflections. Therefore, a scale-selective wave-absorbing layer is imposed by adding the Rayleigh damping terms

$$-\nu(z)(\mathbf{v} - \mathbf{v}^\ell) \quad \text{and} \quad -\nu(z)\theta$$

to the right-hand sides of (1) and (2), respectively. Here $\mathbf{v}^\ell$ represents only the large-scale components of the evolving velocity field. They are computed at each time step by Fourier transforming the u and v fields over the doubly periodic domain at each horizontal level within the sponge layer, filtering out all modes with wavelengths shorter than $L/4 = 450$ km, and transforming the filtered results back to physical space. The large-scale vertical velocity w^ℓ is set to 0 for consistency with the rigid-lid condition ($w = 0$) at the top of the sponge, and because the large-scale vertical velocities forced by the topography are extremely small. The large-scale potential temperature perturbations θ^ℓ are also set to 0 for consistency with $w^\ell = 0$. The depth of the sponge and the strength of the damping were empirically tuned to minimize reflections, starting with values suggested by the analysis of Klemp and Lilly (1978). The Rayleigh damping coefficient ν is zero below $z = 16$ km and increases with height throughout the 16-km deep sponge layer according to (29) of Durran and Klemp (1983) with $\alpha = 2.5 \times 10^{-3}$ s^{-1}.

3. Wave and momentum flux evolution

The large-scale flow [which is not exactly parallel to the isobars due to the enforcement of the nonlinear balance relation (4)] is strictly westerly along an east–west line through the center of the mountain ($y = L/2$), and at the crest its velocity U_{2d} varies with time such that

$$U_{2d}(t) = u_0\left[1 - \cos\left(\frac{2\pi}{\tau}t\right)\right].$$

Thus, the nonlinearity parameter $\varepsilon = Nh/U$ decreases from infinity to a minimum value of $Nh/(2u_0)$ during the accelerating phase ($0 \le \tau/2$), and then subsequently increases back to infinity during the decelerating phase.

Figure 2 shows the perturbation horizontal velocity field ($u + u_0 - U_{2d}$) in a vertical cross section along $y = L/2$ at various times throughout the flow evolution. These waves are forced by a 250-m-high mountain, so the minimum value of ε is 0.125 and the waves are approximately linear throughout the period of strongest wave activity. As the wind across the ridge increases, waves develop and propagate upward. There is a pronounced asymmetry in the wave response between the accelerating and decelerating phases of the background flow. Note in particular, the differences between Figs. 2b and 2e, which correspond to 2 times at which the mean cross-mountain flow and the values of ε are identical. The downstream–upstream variations in the position of the waves shown in Fig. 2 is similar, though less pronounced, than that evident in Fig. 7 of Lott and Teitelbaum (1993a). Larger downstream–upstream shifts were obtained by Lott and Teitelbaum because they considered a more rapidly varying large-scale flow for which the stationarity parameter

$$\gamma \equiv \frac{u_0\tau}{a} = 21.6, \tag{5}$$

as compared with $\gamma = 100$ here.[2]

[2] Lott and Teitelbaum define γ on the basis of the maximum wind, which introduces a factor of 2 difference between in the numerical values given here and those reported in their paper.

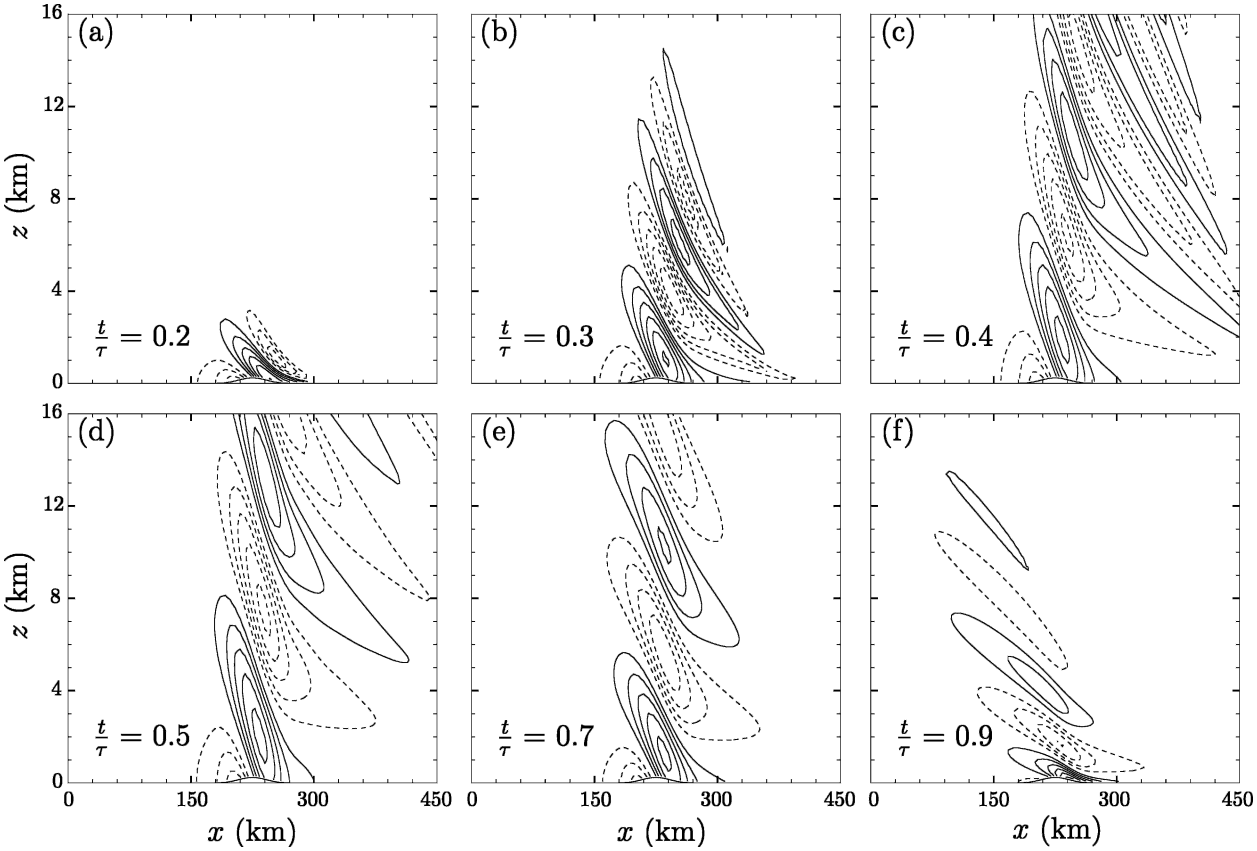

FIG. 2. Vertical cross sections at $y = L/2$ showing the perturbation horizontal velocity forced by a 250-m-high ridge at times (a) 10, (b) 15, (c) 20, (d) 25, (e) 35, and (f) 45 h. The time normalized by the period of the large-scale flow (t/τ) is given in the lower left of each panel.

The Rossby number for the cross-mountain flow $U_{2d}/(fa)$, which rises to 11 at $t = \tau/2$, is sufficiently large that, as a first approximation, the direct influence of rotational effects on the wave dynamics may be neglected during the period when the mountain waves are most active. The minimum ratio of the characteristic horizontal and vertical scales in these waves (Na/U_{2d}) is nine, so at all times the waves are approximately hydrostatic. Thus, if the waves were steady and three-dimensional effects are neglected near the center of the finite ridge, the group velocity would be directed straight upward and all the energy in the disturbance would be confined over the mountain. As apparent in Fig. 2, despite the slow time scale of the mean-flow variation, the waves are generally not close to steady state.

The mean-flow variations are sufficiently gradual in space and time, and the mountain is sufficiently low, that the basic properties of the waves shown in Fig. 2 can be understood using the Wentzel-Kramers-Brillouin (WKB) approximation for linear two-dimensional, nonrotating, hydrostatic Boussinesq gravity waves. For a basic state with constant stability N and horizontal wind speed $U_{2d} > 0$, mountain waves of the form $\exp[i(kx + mz - \omega t)]$ satisfy the dispersion relation

$$\omega = \left(U_{2d} - \frac{N}{m}\right)k. \tag{6}$$

Here k and m are assumed positive so that the wave energy propagates upward and upstream relative to the large-scale flow, as may be verified by noting that

$$\mathbf{c}_g = (c_{g_x}, c_{g_z}) = \left(\frac{\partial\omega}{\partial k}, \frac{\partial\omega}{\partial m}\right) = \left(U_{2d} - \frac{N}{m}, \frac{Nk}{m^2}\right). \tag{7}$$

Using (6) and (7), the stationarity parameter γ may be alternatively interpreted as the ratio of the time scale for variations in the large-scale forcing to the time scale for vertical propagation of the mountain wave, since the time required for a steady mountain wave in a mean flow of strength u_0 and horizontal scale $2\pi/a$ to propagate one vertical wavelength is

$$\frac{2\pi/m}{c_{g_z}} = \frac{2\pi m}{Nk} = \frac{2\pi(N/u_0)}{N(2\pi/a)} = \frac{a}{u_0}.$$

The slow variations of the large-scale flow may be exploited using ray-tracing theory to follow individual wave packets after they are launched by the mountain. As will be demonstrated later in connection with Fig. 10f, the wave-induced cross-mountain pressure drag in this simulation at any given time t_i is very close to that which would be computed using linear theory for steady-state waves in the uniform wind $U_{2d}(t_i)$. A wave packet launched at time t_i is therefore initialized with the same properties as a steady linear 2D mountain wave in a mean westerly flow at speed $U_i \equiv U_{2d}(t_i)$. Following a wave packet in the x–z plane of symmetry at $y = L/2$, ray tracing theory (Lighthill 1978) predicts that

$$\frac{D_g k}{Dt} = -\frac{\partial \omega}{\partial x}, \tag{8}$$

and

$$\frac{D_g m}{Dt} = -\frac{\partial \omega}{\partial z}, \tag{9}$$

where

$$\frac{D_g}{Dt} = \frac{\partial}{\partial t} + \mathbf{c}_g \cdot \boldsymbol{\nabla}.$$

Since the background flow and stratification are constant with height, $\partial\omega/\partial z = 0$, and the initial vertical wavenumber for the steady mountain wave N/U_i is conserved following the packet. Substituting this initial wavenumber for m in (6) and (7), it follows that for a packet launched at time t_i

$$\omega = (U_{2d} - U_i)k, \tag{10}$$

and

$$\mathbf{c}_g = \left(U_{2d} - U_i, \frac{U_i^2}{N} k\right). \tag{11}$$

The preceding may be used to explain many of the features evident in Fig. 2. The horizontal group velocity of each wave packet is initially zero, but increases with time up to $t = \tau/2$; thus wave energy appears downstream of the mountain in Figs. 2a–d. During the decelerating phase almost all waves eventually develop negative c_{g_x}, so that the disturbance shifts back over the mountain in Fig. 2e and even appears upstream of the ridge in Fig. 2f. The vertical wavelength of the disturbance near the mountain is smaller when U_{2d} is small (see particularly Figs. 2a,f) and increases to a maximum at $t = \tau/2$ (Fig. 2d). In a linear hydrostatic steady-state mountain wave, the horizontal wavelength is determined by the topography independent of the cross-mountain wind speed, and very near the surface the dominant horizontal wavelength appears to be constant with time. In the upper part of the domain, on the other hand, the dominant horizontal wavelength is relatively short early in the accelerating phase (Fig. 2b) and gradually lengthens throughout the remainder of the simulation.

Two factors contribute to the changes in horizontal wavelength aloft. First as implied by (11), the shorter waves propagate upward faster (larger c_{g_z}), so early in the accelerating phase the longer wavelength components have not had sufficient time to reach higher altitudes. The second factor is that the horizontal wavelength of each packet is modified by the changes in the background flow. In particular, substituting (6) into (8) yields

$$\frac{D_g k}{Dt} = -k\frac{\partial U_{2d}}{\partial x}, \tag{12}$$

implying that the horizontal wavenumber of the packets increases during the accelerating phase. Conversely, k decreases for $t > \tau/2$ as the mountain waves are stretched by a background flow whose speed increases with distance downstream of the mountain. Although not apparent in the snapshots in Fig. 2, the phase lines appear to move up and to the right during the accelerating phase and then reverse, moving down and to the left during the decelerating phase. For an individual wave packet, the phase lines move at the phase speed c_p in the direction normal to the wave vector $\mathbf{K}$, such that

$$c_p \frac{\mathbf{K}}{|\mathbf{K}|} = \frac{\omega}{(k^2 + m^2)^{1/2}} \frac{(k, m)}{(k^2 + m^2)^{1/2}} = (U_{2d} - U_i)\frac{k}{k^2 + m^2}(k, m).$$

Thus, when the environmental wind exceeds the speed of the flow at the time the packet was generated, its phase moves downstream and upward. This takes place during the accelerating phase ($t < \tau/2$). On the other hand, late in the decelerating phase almost all packets are in an environment for which $U_{2d} - U_i < 0$ and the phase lines move upstream and toward the ground.

Now consider the momentum flux transported by the mountain waves. Let $\langle F \rangle$ denote the integral of the function F over a horizontal plane spanning the periodic computational domain,

$$\langle F \rangle = \int_0^L \int_0^L F\, dx\, dy,$$

and let ρ_0 be a constant reference density of 1 kg m^{-3}. Figure 3b shows the $z - t$ distribution of the vertical flux of x-component momentum $\langle \rho_0 uw \rangle$ for the simula-

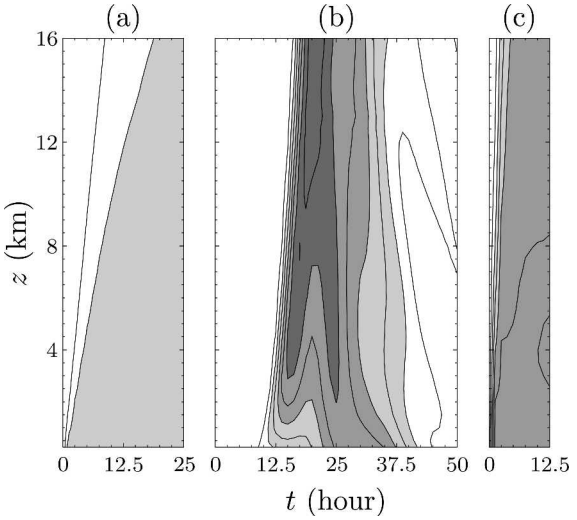

FIG. 3. Horizontally integrated momentum flux $\langle \rho_0 uw \rangle$ as a function of time and height for a mountain with $h = 250$ m in a large-scale flow for which (a) $(U, V) = (10, 0)$ m s^{-1}, (b) the flow is periodic and given at $t = 0$ by the pattern in Fig. 1, and (c) $(U, V) = (20, 0)$ m s^{-1}. The contour interval is 4×10^8 N, and gray-scale shadings, ordered by increasing intensity, indicate values less than -8×10^8, -16×10^8, and -24×10^8 N.

tion shown in Fig. 2. A pronounced difference between the momentum fluxes in the accelerating and decelerating phases of the large-scale flow is visible in Fig. 3b, with much stronger momentum flux occurring during the accelerating phase. The strongest momentum fluxes are found in the layer $10 \leq z \leq 16$ km around $t = 20$ h. Moreover, during the period $11 \leq t \leq 26$ h, the momentum fluxes decrease (become more negative) with height through the lowest 5 km, implying that over a 15-h period gravity wave drag is exerting an accelerative force on the mean flow throughout this layer.

The situation shown in Fig. 3b is very different from that obtained when the mean flow is instantaneously started from rest and then held at a constant value. Examples of the momentum fluxes in two such constant-wind cases are shown in Figs. 3a,c, which are for simulations identical to that in Fig. 3b except that the background flow is constant with $V = 0$ and $U = 10$ (the time mean of U_{2d}) or 20 m s^{-1} (the maximum of U_{2d}). Both time axes in Figs. 3a,c terminate at a nondimensional time $Ut/a = 50$ identical to that associated with the accelerating phase of the slowly evolving flow in Fig. 3b. The maximum momentum flux generated by the waves in the slowly evolving flow is stronger than in the cases with constant background flow. This is expected for the case with $U = 10$ m s^{-1} because the magnitude of the momentum flux in steady linear mountain waves is proportional to the speed of the mean flow, but $\langle \rho_0 uw \rangle$ in the slowly evolving flow is also 1.4 times stronger than that in the case with $U = \max(U_{2d}) = 20$ m s^{-1}. Also, in contrast to the case for a slowly evolving flow, the vertical gradient of $\langle \rho_0 uw \rangle$ in both of the constant-wind cases is negative at all levels during the period of mountain-wave development, so the net wave-induced forcing on the mean flow is everywhere decelerative. Finally, the waves approach steady state, and the momentum flux becomes almost uniform with height at relatively early nondimensional times in both of the constant-wind cases.

The evolution of the momentum flux shown in Fig. 3b is also rather different from what might nominally be expected from steady-state mountain-wave theory. According to linear theory, the cross-mountain pressure drag and the pseudomomentum associated with wave packets generated by the topography increase as the cross-mountain wind increases. One might therefore suppose that near the surface the vertical momentum-flux gradient would be positive (momentum flux becoming less negative with height) until the time of maximum wind, and then turn negative for $t > \tau/2$ as the cross-mountain flow relaxes back to zero. Clearly, this is not the behavior shown in Fig. 3b.

4. Analysis of the momentum flux distribution

The processes responsible for creating the highly structured momentum flux distribution in Fig. 3b will be examined in the context of linear theory. To better assess the agreement between our theoretical constructions and the results of the numerical model we consider a slightly more linear problem in which the mountain height is reduced to 125 m, for which the nonlinearity parameter ε is 1/16 at the time of maximum wind.[3] The momentum flux $\langle \rho_0 uw \rangle$ distribution for this case (Fig. 4a) looks similar to that for the 250-m case (Fig. 3b), except that regions of positive momentum flux appear for $t > 45$ h.

The positive momentum fluxes in Fig. 4a are produced by a weak large-scale component of the mountain-wave response that projects onto the large-scale flow. Recall that (U, V) is the large-scale velocity field that would be present if there was no mountain, and define a mesoscale velocity field u' such that $u'(x, y, z, t) = u(x, y, z, t) + u_0 - U(x, y, t)$. The total vertical momentum flux is the sum of the large-scale flux $\langle \rho_0 Uw \rangle$ and the mesoscale flux $\langle \rho_0 u'w \rangle$. These large-

[3] A simulation in which the mountain height is reduced to 12.5 m generates fields of the perturbation variables that are almost identical to those in the h = 125 m case, except their amplitude is reduced by a factor of 10, which confirms that the 125-m-high mountain is producing an essentially linear result.

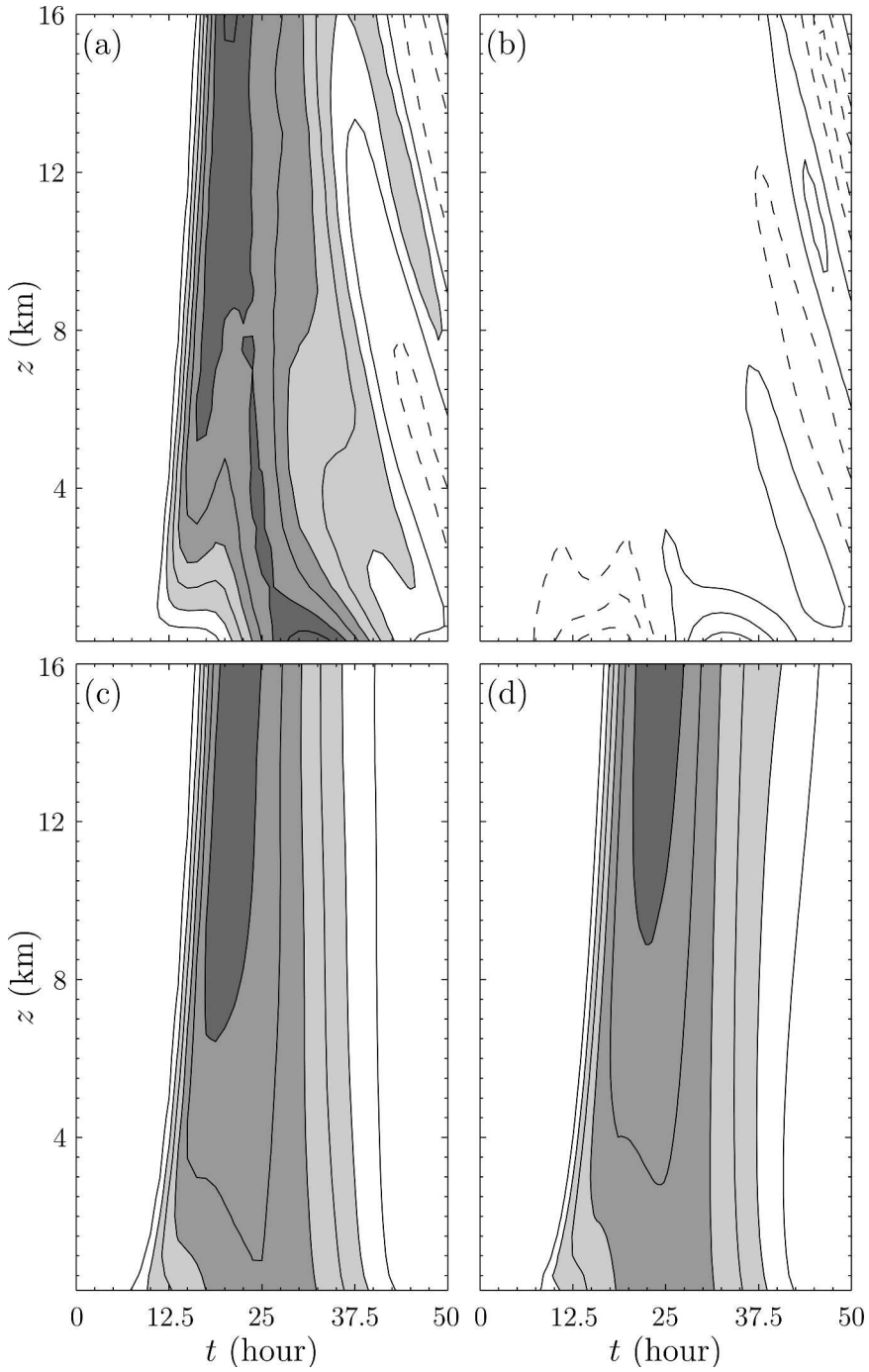

FIG. 4. Horizontally integrated momentum flux as a function of t and z for the $h = 125$ m simulation: (a) $\langle \rho_0 uw \rangle$, (b) $\langle \rho_0 Uw \rangle$, (c) $\langle \rho_0 u'w \rangle$, and (d) idealized reconstruction by using ray-tracing theory. The contour interval is 10^8 N; positive values are dashed and gray shadings, ordered by increasing intensity, indicate values less than -2×10^8, -4×10^8, and -6×10^8 N.

scale and mesoscale contributions to the momentum flux are plotted as a function of z and t in Figs. 4b,c. Clearly all the positive flux is produced by the large-scale contribution. Because of the orthogonality of the Fourier modes over our doubly periodic domain, the large-scale flux is produced entirely by the interaction of the synoptic-scale flow itself with the gravity wave having the same square-wave structure ($k = l = 2\pi/L$)

as the synoptic-scale flow.[4] The large-scale momentum flux is most significant when the mountain is low, because $\langle \rho_0 Uw \rangle$ scales like the mountain height h, whereas the mesoscale flux scales like h^2; thus the large-scale contribution is less apparent in Fig. 3b. Throughout the remainder of this section, we focus on the mesoscale momentum flux $\langle \rho_0 u'w \rangle$, which is produced entirely by the mountain waves themselves and dominates the total momentum flux in more nonlinear problems.

Figure 4d shows a reconstruction of the vertical momentum flux distribution obtained through WKB ray tracing and the conservation of wave action using an approach that will be described shortly. The agreement between the model result (Fig. 4c) and this reconstruction is rather good, implying that these theoretical tools can be used to understand both the marked difference in momentum fluxes in the accelerating and decelerating phases of the flow and the reversal of the vertical momentum flux gradient in the lower troposphere around hour 15.

Wave packets generated at the mountain propagate upward through a large-scale flow $\mathbf{U} = (U, V, 0)$ that changes slowly with respect to x, y, and t. The wave action density $\mathcal{A}$ associated with each packet is governed by the relation

$$\frac{\partial \mathcal{A}}{\partial t} + \nabla \cdot (\mathcal{A}\mathbf{c}_g) = 0, \tag{13}$$

where $\mathcal{A} = \mathcal{E}/\hat{\omega}; \hat{\omega} = \omega - \mathbf{U} \cdot \mathbf{K}$ is the intrinsic frequency, and $\mathcal{E}$ is the wave energy density (Bretherton and Garrett 1968; Whitham 1974). For hydrostatic Boussinesq internal gravity waves

$$\mathcal{E} = \frac{\rho_0}{2}\left(\overline{\mathbf{u}'^2} + \frac{\overline{b'^2}}{N^2}\right), \tag{14}$$

where $\mathbf{u}' = (u + u_0 - U, v - V, 0)$, $b' = g(\theta - \theta_r)/\theta_0$, $N^2 = (g/\theta_0)d\theta_r/dz$, and the overbar denotes an average over one cycle of the wave. The rays along which wave packets propagate away from the crest of the mountain at time t_i are the solutions to

$$\frac{d\mathbf{x}}{dt} = \mathbf{c}_g, \tag{15}$$

subject to the initial condition $\mathbf{x}(t_i) = (x_0, L/2, 0)$. Because of the y symmetry of the flow, those packets with y wavenumber l equal to zero remain in the $y = L/2$ plane, and since most of the waves forced by the $\beta = 5$ ridge have wave fronts approximately parallel to the y axis, we temporarily focus on waves with $l = 0$. The maximum momentum flux in two-dimensional (x–z) waves forced by the ridge cross section parallel to the x axis, $h_s(x, L/2)$, occurs approximately at wavenumber $\tilde{k} = 13\ (2\pi/L)$ or wavelength $\tilde{\lambda} \sim 138$ km. Rays for packets initialized at $t_i = 6, 7, \ldots, 50$ h with wave vectors corresponding to steady two-dimensional mountain waves in a mean flow U_i, that is, with $\tilde{\mathbf{K}} = (\tilde{k}, 0, N/U)$, are illustrated in Fig. 5. Rays for $t \leq 5$ h are associated with packets of weakly forced waves that do not transport significant momentum, and these rays are omitted for clarity.

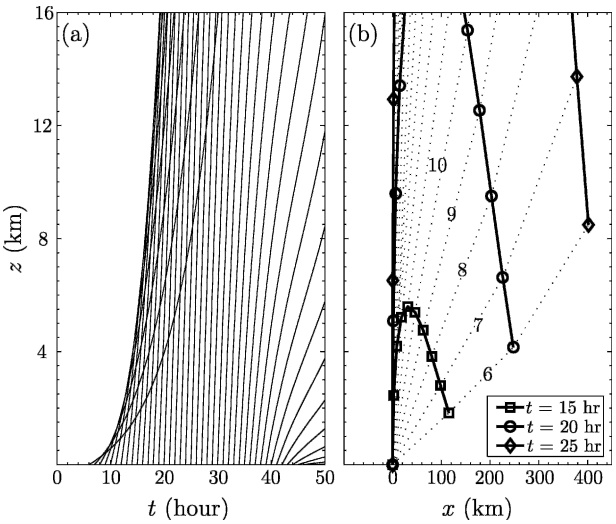

FIG. 5. Ray paths for packets launched at hourly intervals from the ridge crest with initial wavenumber $\tilde{\mathbf{K}}$ (a) projected onto the z–t plane and (b) projected onto the x–z plane (dotted lines labeled according to the time they were launched). In (b) the symbols connected by solid lines show the location of previously launched packets at $t = 15$, 20, and 25 h, and the origin ($x = 0$) is shifted to coincide with the ridge crest.

The projection of each ray onto the $z - t$ plane is plotted in Fig. 5a. Rays emanating from the surface early and late in the simulation ascend at a shallow angle because the vertical group velocity $U_i^2 k/N$ is small if wave packets are initialized while the large-scale winds are weak. Conversely, rays rise at a steep angle near the time of maximum wind ($t = 25$ h). The relatively small vertical group velocities of rays launched shortly after $t = 6$ h eventually increase due to the variations in k along the ray path as implied by (8). Lott and Teitelbaum (1993a,b) presented diagrams similar to Fig. 5a to explain variations in wave amplitude and position in a slowly varying flow. Here we use Fig. 5a to help explain the mesoscale momentum flux distribution shown in Fig. 4c. The onset of significant momentum flux at some vertical level in Fig. 4c is closely associated with the arrival of the curve formed by the left edge of

[4] This was verified by Fourier transforming the vertical velocity to isolate the large-scale square-wave contribution $w_{1,1}$ and comparing the virtually identical distributions of $\langle \rho_0 U w_{1,1} \rangle$ and $\langle \rho_0 Uw \rangle$.

the union of the ray paths in Fig. 5a. Furthermore, the transition from high to low momentum flux that occurs as mean-flow acceleration gives way to deceleration is well correlated with the transition between the convergence of ray paths in the $z - t$ plane for $t < \tau/2$ and divergence for $t > \tau/2$.

Wave action tends to accumulate aloft during the period of flow acceleration because packets launched later in the acceleration phase have larger vertical group velocities and overtake those launched earlier. Such behavior is illustrated in Fig. 5b, which shows the position in the x–z plane of packets launched from the ridge crest with initial wavenumber $\tilde{\mathbf{K}}$ at various times. The thin dotted lines show the trajectory of each individual packet and are labeled with the time in hours at which the packet was launched. The symbols connected by solid lines show the position of all previously launched packets at a given instant in time, the squares, for example, indicate packet positions at $t = 15$ h. Note that packets launched at 10, 11, and 12 h all arrive at a height of roughly 5.5 km at $t = 15$ h. Figure 5b also shows that the vertical convergence of wave packets is partially compensated by horizontal divergence, so that the wave action density at any given point never becomes unbounded.

A second factor influencing the $z - t$ distribution of momentum flux shown in Fig. 4c is the difference in the wave action between various wave packets arising from the differences in cross-mountain wind speed at the time each packet was launched. Given the wave action density just above the mountain as a function of wavenumber and time, one may use (13) to compute a WKB approximation to the distribution of $\langle \mathcal{A} \rangle$ (z, t) numerically, and connect the result with the $z - t$ momentum-flux distribution as follows. First consider the relation between momentum flux and wave action for a single wave packet. Let $\mathcal{M} = \overline{\rho_0 u' w}$ denote the mesoscale momentum flux averaged over one cycle of the wave, and note that for hydrostatic Boussinesq gravity waves with vertical velocity $\Re\{w_0 \exp[i(kx + ly + mz - \omega t)]\}$,

$$\mathcal{E} = \rho_0 \frac{w_0^2}{2} \left(\frac{m^2}{k^2 + l^2} \right) = - \frac{m}{k} \mathcal{M}, \tag{16}$$

which implies that for these waves,

$$\mathcal{A} = - \frac{m\mathcal{M}}{k\hat{\omega}} = \frac{m^2 \mathcal{M}}{Nk(k^2 + l^2)^{1/2}}, \tag{17}$$

where the last equality is obtained from the dispersion relation for waves propagating upward [implying $\mathrm{sgn}(k) = \mathrm{sgn}(m)$] and westward relative to the mean flow

$$\hat{\omega} = \omega - Uk - Vl = - \frac{N(k^2 + l^2)^{1/2}}{m}.$$

The distribution of $\langle \mathcal{A} \rangle$ (z, t) is estimated by launching a series of wave packets from the mountain crest at regular time intervals δt and following them upward from $\mathbf{x}(t_i) = (x_0, L/2, 0)$ by integrating (15) along with the ray tracing relations for our particular large-scale flow

$$\frac{D_g k}{Dt} = -k \frac{\partial U}{\partial x} - l \frac{\partial V}{\partial x}, \tag{18}$$

$$\frac{D_g l}{Dt} = -k \frac{\partial U}{\partial y} - l \frac{\partial V}{\partial y}, \tag{19}$$

$$\frac{D_g m}{Dt} = 0. \tag{20}$$

The initial wave activity of each packet is assumed to lie within a thin horizontal slab of thickness $c_{g_z} \delta t$ extending throughout the horizontal domain. Using (17), the volume-integrated wave activity at wavenumber (k, l) in the slab just above the surface at the time t_i at which a packet is launched is approximately

$$\langle \mathcal{A}_{k,l} \rangle c_{g_z} \delta t = \frac{m^2 \langle \mathcal{M}_{k,l} \rangle c_{g_z} \delta t}{Nk(k^2 + l^2)^{1/2}},$$

where $\langle \mathcal{M}_{k,l} \rangle$ is the (k, l)th component of the two-dimensional Fourier transform of the mountain-wave momentum flux for linear steady-state flow at speed U_i.

The slab containing the packet is followed upward assuming that the top of the slab moves at the group velocity of the ray launched at t_i and the bottom moves at the group velocity of the ray launched at $t_i + \delta t$. Let $\mathcal{V}$ denote a volume whose boundary $\mathcal{S}$ moves at the group velocity. Integrating (13) over $\mathcal{V}$ using the divergence theorem and the generalized Leibniz theorem, one may obtain the integral form of the wave action conservation law (which is directly analogous to the Lagrangian relation for mass conservation)

$$0 = \int_{\mathcal{V}} \frac{\partial \mathcal{A}}{\partial t} dV + \int_S d\mathbf{S} \cdot \mathbf{c}_g \mathcal{A} = \frac{D_g}{Dt} \left(\int_{\mathcal{V}} \mathcal{A} \, dV \right). \tag{21}$$

For the horizontal slab containing the packet moving upward at the group velocity, (21) reduces to

$$\frac{D_g}{Dt} \left(\int_0^L \int_0^L \int_{z_b}^{z_t} \mathcal{A} \, dz \, dx \, dy \right) = 0, \tag{22}$$

where z_t and z_b denote the heights of the top and bottom of the slab. Thus at some later time t_f, the horizontally integrated wave action for the packet launched at t_i satisfies

$$[\langle \mathcal{A}_{k,l} \rangle |z_t - z_b|]_{t=t_f} = [\langle \mathcal{A}_{k,l} \rangle |z_t - z_b|]_{t=t_i} = [\langle \mathcal{A}_{k,l} \rangle c_{g_z} \delta t]_{t=t_i}.$$

As the slab containing the packet reaches each vertical level on a $z - t$ grid, the wave activity density is con-

verted back to a momentum flux using (17) and the packet values of k and l as determined from (18) and (19), and that momentum flux is distributed via a finite volume formalism in the discretized time domain. Finally the momentum fluxes associated with all packets at a given t and z are summed to obtain $\langle \mathcal{M} \rangle$ (z, t).

The result of this WKB momentum flux reconstruction is plotted in Fig. 4d, which is in reasonably good agreement with the full numerical result shown in Fig. 4c. Note in particular that the WKB reconstruction exhibits the same pronounced enhancement of the vertical momentum flux during the accelerating phase of the synoptic-scale flow and the same region of low-level momentum flux convergence around $t = 15$ h diagnosed from the numerical simulation.

One additional factor influences the acceleration–deceleration asymmetry in the $z - t$ distribution of the momentum flux in Figs. 4c,d, and this factor, which is included in the WKB reconstruction, is the change in the momentum flux carried by individual packets along each ray path. Since wave action is conserved following each packet, (17) implies that any changes in k and l produced through stretching or compression of the waves by variations in the large-scale velocities U and V will be associated with changes in $\mathcal{M}$. (Since there are no vertical variations in the large-scale structure, m is constant.) The changes in $\langle \rho_o u'w \rangle$ are much more sensitive to changes in k than to changes in l because of the extra factor of k in the denominator of (17) and because the elongation of the ridge parallel to the y axis implies that $k \gg l$ for those modes that carry the most momentum flux. While the synoptic-scale flow over the mountain is accelerating, $\partial U/\partial x < 0$ and the first term on the right of (18) acts to increase k along the ray path. The other term in (18), involving $\partial V/\partial x$, is small because V is small for all x in the east–west strip of the domain containing the mountain. The increase in k during the accelerating phase produces an increase in $\mathcal{M}$ that significantly enhances the total momentum flux during the accelerating phase. In fact, some of the wave packets involved in the WKB reconstruction undergo so much compression during the accelerating phase that the WKB assumption for these packets is violated because the ks begin to change significantly within a single horizontal wavelength. The maximum increase in k for these packets was therefore limited according to the criterion described in the appendix.

The relative importance of mean-flow-induced compression and stretching on the overall momentum flux distribution can be assessed by considering another numerical simulation with a spatially uniform time-dependent large-scale flow in which $U = U_{2d}(t)$, $V = 0$. This large-scale flow is geostrophically balanced with respect to a hypothetical north–south pressure gradient that increases and relaxes back to zero over a period of 50 h. The large-scale flow over the crest of the mountain is identical to that generated by the translating square wave, but since there are no spatial variations in U and V (or N), individual wave packets conserve k, l and m, and by (17), $\mathcal{M}$ is also conserved. The $z - t$ distribution of $\langle \rho_o uw \rangle$ from this simulation is shown in Fig. 6a. Although the asymmetry between the momentum flux in the accelerating and decelerating phase and the tendency for the location of the maximum momentum flux to shift above the surface are both apparent in this spatially uniform simulation, the maximum momentum flux is substantially weaker (only 80%) of that in the simulation with the translating synoptic-scale square wave (Fig. 4c).

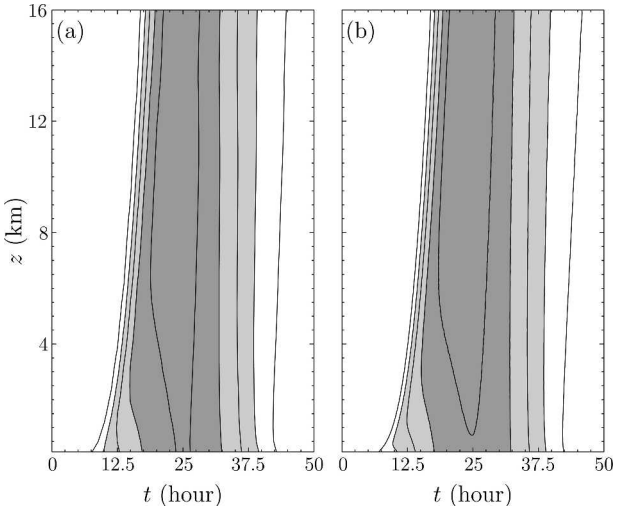

FIG. 6. Horizontally integrated momentum flux as a function of t and z for a mountain with $h = 125$ m (a) from the spatially uniform simulation and (b) reconstructed using WKB ray tracing and the conservation of $\mathcal{M}$. Contour interval and shading as in Fig. 4.

WKB ray tracing can also be used to reconstruct the $z - t$ distribution of $\langle \rho_o u'w \rangle$ in the spatially uniform simulation using the procedure just described except that $\mathcal{A}$ is replaced by $\mathcal{M}$ in the underlying conservation relation (13). As evident from Fig. 6, this reconstruction gives a very good approximation to the flux from the numerical simulation.

One final way to assess the influence of mean flow stretching and compression on the mountain waves in the simulation with the translating square wave is by comparing plots of perturbation horizontal velocity for this case with corresponding plots from the spatially uniform simulation [the case $U = U_{2d}(t)$, $V = 0$]. Figures 7a,c show vertical cross sections of u' along the line $y = L/2$ at $t = 17.5$ h from the translating-square-wave

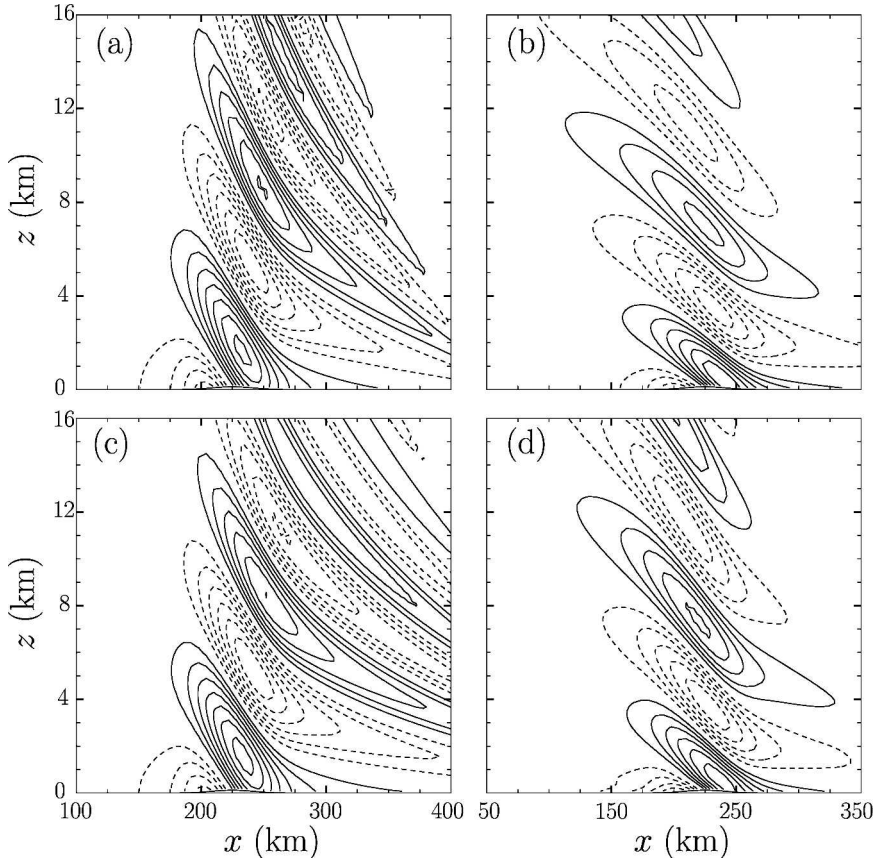

FIG. 7. Vertical cross sections u' at $y = L/2$ forced by a 125-m-high ridge in the translating square-wave simulation at times (a) 17.5 and (b) 40 h, and in the spatially uniform simulation at (c) 17.5 and (d) 40 h. The contour interval is 0.15 m s^{-1}; the zero contour is omitted.

and the spatially uniform simulations, respectively. Although there are substantial similarities, particularly throughout the lower levels, near the upper boundary larger perturbation amplitudes and shorter wavelength perturbations are clearly discernible in the translating-square-wave simulation. Conversely, during the decelerating phase at $t = 40$ h, the translating-square-wave simulation (Fig. 7b) has longer waves and weaker perturbation amplitudes near the upper boundary than does the spatially uniform case (Fig. 7d). These differences are consistent with the conservation of wave action and the tendency of k to increase (or decrease) when the packets are in regions with $\partial U/\partial x < 0$ (or $\partial U/\partial x > 0$).

5. Slower evolution and higher ridges

The preceding results suggest the vertical profile of mountain-wave-induced momentum flux in a flow evolving on a 2-day time scale can be very different from that predicted using steady-state theory and the instantaneous flow velocities above the mountain. How slow does the large-scale evolution need to be before the steady-state assumption becomes accurate? Some indication can be obtained by increasing the spatial scale of the square wave so that it takes longer to sweep across the mountain.

Figure 8 shows estimated $z - t$ distributions of $\langle \rho_0 u' w \rangle$ for three cases of flow over a 125-m-high ridge in which the period of the synoptic-scale system is 100, 150, and 200 h (corresponding to stationarity parameters $\gamma = 200$, 300, or 400). These fluxes are only estimates since they were constructed using WKB theory and the conservation of wave action rather than direct numerical simulation because it is too computationally expensive to increase the domain to the size required for complete simulations. Both the $\gamma = 200$ and $\gamma = 300$ cases show strong evidence of nonsteadiness, including significant asymmetries between the momentum fluxes during the accelerating and decelerating phases of the synoptic-scale flow, with enhanced momentum fluxes aloft when the cross-mountain flow is increasing (Figs.

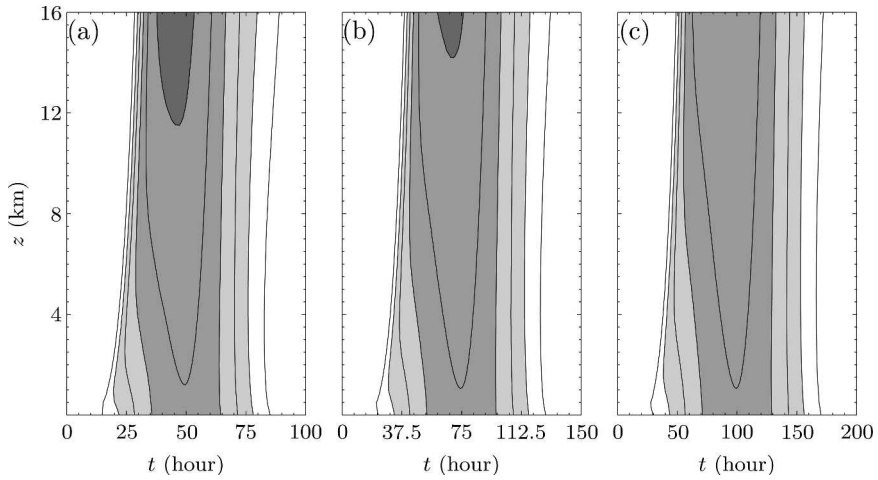

FIG. 8. WKB estimate of $\langle \rho_0 u'w \rangle$ for a 125-m-high ridge as a function of t and z for synoptic-scale periods of (a) 100 h ($\gamma = 200$), (b) 150 h ($\gamma = 300$), and (c) 200 h ($\gamma = 400$). Contour interval and shading as in Fig. 4.

8a,b). As in the $\gamma = 50$ case discussed previously, when the momentum fluxes aloft are enhanced, the low-level fluxes are convergent and provide forcing to accelerate the large-scale flow. Even when $\gamma = 400$, corresponding to synoptic-scale evolution over a period greater than eight days, there is still some asymmetry between the accelerating and decelerating phases in the momentum fluxes aloft (Fig. 8c). The results shown in Fig. 8 suggest that mean-flow variations may exert a nontrivial influence on mountain-wave-induced momentum fluxes on essentially all meteorologically relevant time scales.

The character of the momentum flux generated by higher ridges is illustrated in Fig. 9, which shows $z - t$ plots of $\langle \rho_0 u'w \rangle$ normalized by the flux for the linear solution for the same mountain in a uniform steady flow with $U = U_{2d}(t = 25) = 20$ m s^{-1} and $V = 0$. In all cases $\gamma = 100$. The minimum value of the nonlinearity parameter $\varepsilon = Nh/U_{2d}$ ranges from 0.125 for $h = 250$ m to 0.5 for $h = 1$ km. Around hours 15 to 20 during the accelerating phase of the synoptic-scale flow, the momentum fluxes aloft are significantly larger than those predicted by the linear steady-state model. When $h = 250$ m (Fig. 9a), the flux exceeds the maximum linear steady-state flux (which would not occur until $t = 25$ h) by more than 25%. As the height of the ridge increases, this enhancement becomes much stronger, increasing to more than 125% when $h = 1000$ m (Fig. 9d). In contrast, there is very little nonlinear enhancement during most of the deceleration phase.

The maximum value of the subgrid-scale eddy diffusivity over each horizontal plane in the domain is also plotted in Fig. 9 (dashed contours). When $h = 250$ m, there is no subgrid-scale mixing except at low levels near the very end of the simulation. For all the other cases, significant values of low-level subgrid-scale mixing occur during those periods of large-scale flow acceleration and deceleration when the local value of ε is large, except that there is no mixing very early in any simulation because mountain waves have not yet developed in the blocked flow. Not surprisingly, the period of time over which subgrid-scale mixing is active, and the maximum strength of that mixing, increases with increases in the mountain height. In the cases with higher mountains, the mixing extends to higher altitudes and persists closer to the time of maximum cross-mountain winds during the accelerating phase of the synoptic-scale flow.

The results in Fig. 9 demonstrate that, at least for mountain heights up to 1 km, nonlinear processes reinforce the tendency for accelerating synoptic-scale cross-mountain flows to generate enhanced momentum fluxes aloft and low-level momentum flux convergence. Also of note is that around $t = 20$ h in the 1000-m-high-mountain case (Fig. 9d), the magnitude of the momentum flux is larger above the wave-breaking region (at $z = 7$ km) than below (at $z = 1$ km)!

Another perspective on the influence of nonlinear processes is provided in Fig. 10, which shows the evolution of the normalized cross-mountain pressure drag

$$D = -\frac{1}{D_l}\int_0^L \int_0^L P\frac{\partial h_s}{\partial x}\,dx\,dy\bigg|_{z=h_s},$$

where D_l is the drag for the steady-state linear solution for the same finite-length ridge with $U = U_{2d}(t = 25)$ and $V = 0$. There are two contributions to D, a mesoscale component D' produced by the pressure pertur-

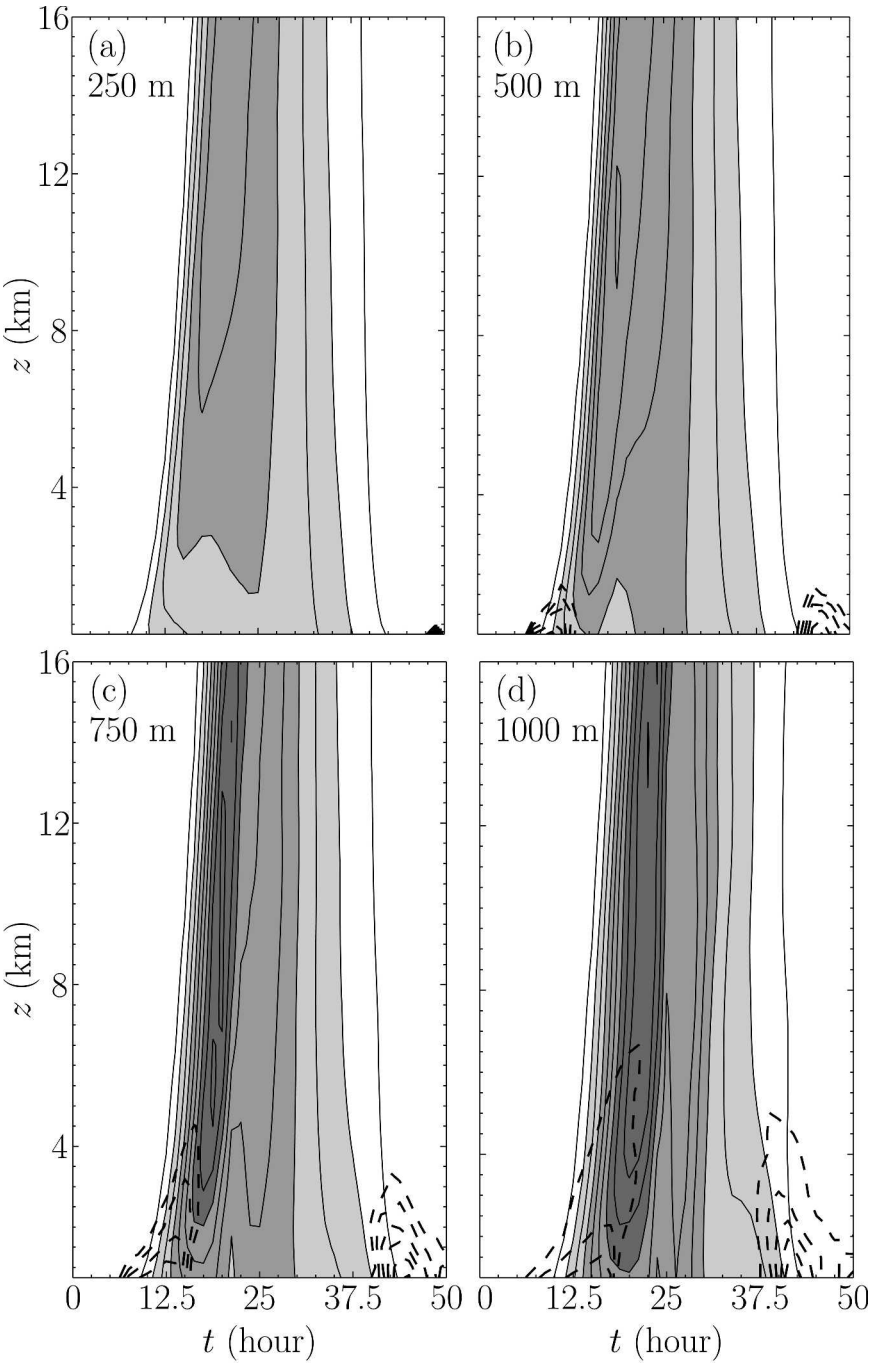

FIG. 9. Momentum flux $\langle \rho_0 u'w \rangle$ normalized by the flux for the linear steady-state solution driven by the maximum cross-mountain flow of 20 m s^{-1} (shading and solid contours) and domain maximum subgrid-scale diffusivity (dashed) as a function of t and z for ridges of height (a) $h = 250$, (b) 500, (c) 750, and (d) 1000 m. The contour interval for the momentum flux is 0.25, with shading ordered by intensity at thresholds of 0.5, 1.0, and 1.75. Contour intervals for the diffusivity are (a) 0.4, (b) 1.4, (c) 2.5, and (d) 5 m^2 s^{-1}.

bations induced by the interaction of the flow with the topography, and a synoptic-scale component D_s resulting from asymmetries in the background pressure field about coordinate axes through the center of the ridge. These asymmetries arise because the synoptic-scale pressure is in nonlinear balance with the square wave in the velocity field, so the lows are stronger than the highs and the background pressure drag on the topog-

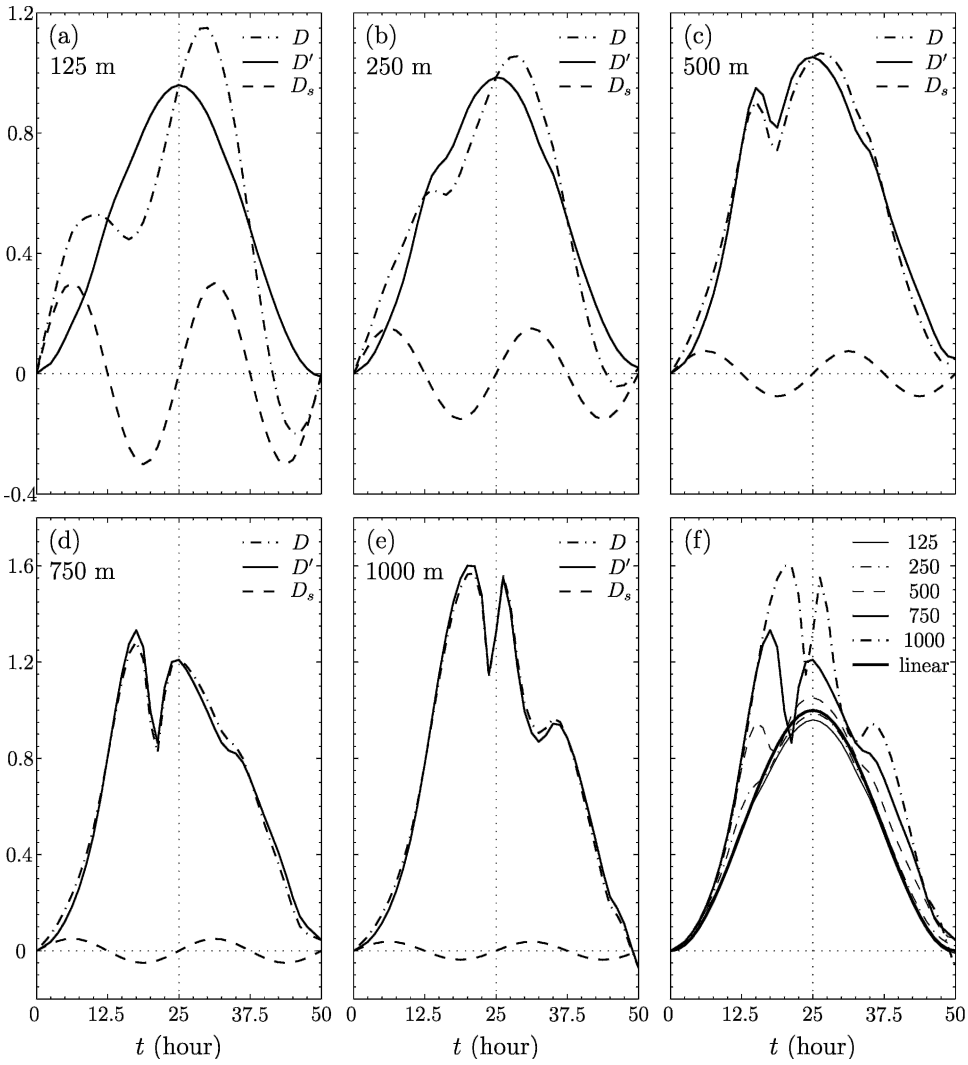

FIG. 10. Time evolution of normalized pressure drag (D: full pressure drag, D_s: synoptic-scale pressure drag, D': mesoscale pressure drag). The normalization is done by dividing each value by the pressure drag for the linear steady-state solution generated by a uniform 20 m s^{-1} flow over the same 3D ridge. Plots of drags for mountain heights of (a) 125, (b) 250, (c) 500, (d) 750, and (e) 1000 m, and (f) D' for all five cases and the linear solution are compared.

raphy north of the centerline at $y = L/2$ does not cancel the drag south of that line. Therefore, as evidenced by the dashed lines in Figs. 10a–e, D_s oscillates with a period one-half that of the synoptic-scale flow. Figure 10 also shows that the contribution of D_s to the total pressure drag D (dash–dotted curve) drops rapidly as h increases, since D_s/D' scales like $1/h$.

Figure 10a shows plots of D, D', and D_s for the simulation with $h = 125$ m. Linear theory for steady-state mountain waves predicts that the pressure drag should be proportional to the cross-mountain wind speed, and this is the case for the 125-m high mountain: the mesoscale drag D' (solid curve) is a roughly sinusoidal function of time and is in phase with $U_{2d}(t)$. Indeed as shown in Fig. 10f, the magnitude of D' is very close to that predicted using the linear steady-state model and the instantaneous cross-mountain wind speed. This justifies our method for determining the initial momentum fluxes carried by each wave packet in the WKB reconstructions of the momentum flux distribution in Figs. 4d, 6b, and 8.[5] On the other hand, when $h = 500$ m, a

[5] Bannon and Zehnder (1985) found that the pressure drag in their time-dependent linear solution could deviate significantly from predictions computed using the instantaneous wind in a linear steady-state model, but they considered situations with much smaller Rossby numbers and much faster time evolution, and they did not solve an initial-value problem.

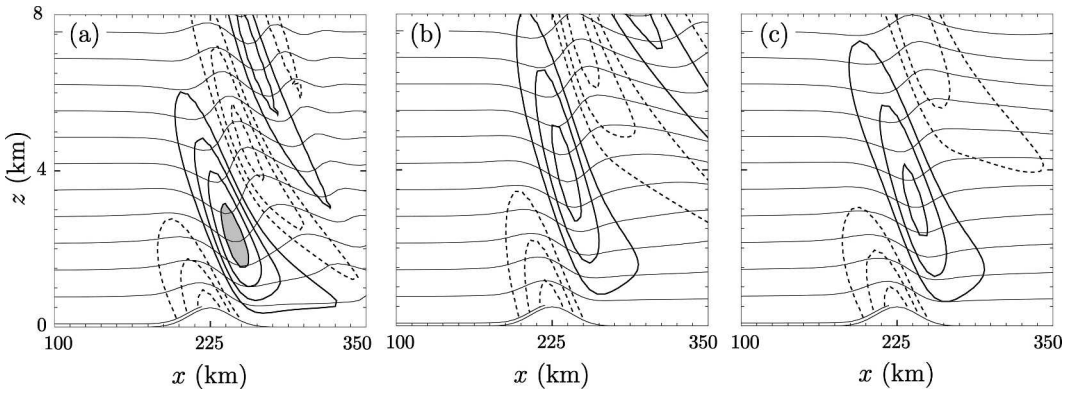

FIG. 11. Three x–z cross sections along the centerline of the mountain showing zonal velocity perturbation (u') in thick lines, and the potential temperature field in thin lines for $h = 500$ m, for $t =$ (a) 15, (b) 18.75, and (c) 35 h. The contour intervals are 1 m s^{-1} and 2 K.

significant enhancement of the drag, relative to that predicted by steady-state linear theory, occurs around $t = 15$ h. Some hint of this enhancement is also visible in the 250-m simulation. No significant enhancement is seen when the same value of ε occurs during the deceleration phase at $t = 35$ h. Note that the instantaneous value of Nh/U is identical at $t = 15$ and 35 h, but the pressure drag is 35% higher during the acceleration phase.

The nonlinear enhancement of the drag around $t = 15$ h over the 500-m-high mountain is not produced by wave breaking, which is not occurring, but rather by the accumulation over the mountain of nonlinear packets that were launched earlier in the acceleration phase when ε was greater than Nh/U ($t = 15$) = 0.42. Figure 11 shows contours of perturbation potential temperature and isentropes of full potential temperature along a vertical cross section at $y = L/2$ for the 500-m mountain simulation at $t = 15$, 18.75, and 35 h. At $t = 15$ (Fig. 11a), the isentropes in the zone of flow deceleration between $z = 2$ and 4 km show the characteristic nonlinear steepening found in previous solutions to Long's equation (Smith 1977; Lilly and Klemp 1979). At the other two times, the isentropes in the lowest zone of decelerated flow are considerably less steep. The steeper isentropes at $t = 15$ h are associated with warmer potential temperature perturbations in the lee trough and, through the hydrostatic relation, lower leeside pressure perturbations that are responsible for the increased drag.

Further nonlinear enhancement of the pressure drag and the asymmetry between the accelerating and decelerating phases of the mean flow is evident in Figs. 10d,e, which are plots of the drag over mountains 750 m and 1 km high. As suggested by the contours of subgrid-scale mixing shown in Figs. 9c,d, significant wave breaking occurs in both of these simulations, and except around the time of maximum wind, this provides the mechanism by which the drag is enhanced relative to that predicted by linear theory (Peltier and Clark 1979). In both cases, the first period of enhanced drag (see also Fig. 10f) terminates when wave breaking ceases in response to the strengthening cross-mountain flow (at $t = 17.5$ h when $h = 750$ m and at $t = 20$ h when $h = 1$ km). Similarly, the modest nonlinear enhancement of the drag later in the decelerating phase is primarily due the redevelopment of breaking waves aloft.

The enhancement of the drag at the time of maximum wind apparent in Figs. 10d,e is not, however, associated with wave breaking. Rather the enhanced drag is due to a transient increase in the amplitude of the laminar waves aloft roughly similar to that illustrated in Fig. 11. At the time of maximum wind in the $h = 1$ km case, $\varepsilon = 0.5$, and the drag generated by the slowly varying nonlinear flow is 1.55 times that produced by the steady linear solution. This may be compared with the factor of 1.22 by which the drag for the steady $\varepsilon = 0.5$ solution is enhanced relative to the linear solution for the same 3D ridge [calculable from Fig. 2a in Epifanio and Durran (2001)] and the factor of roughly 1.2 by which the drag in Long's solution for the $\varepsilon = 0.5$ case is increased relative to the linear solution for 2D flow over a Witch-of-Agnesi mountain (Lilly and Klemp 1979).

6. Conclusions

Mountain-wave momentum fluxes in a slowly varying synoptic-scale flow have been shown to be dramatically different from those that would be determined using steady-state models and the instantaneous vertical distributions of N and U, even when the large-scale winds

evolve on a time scale as slow as 2 to 4 days. These results were established through direct numerical simulation and theoretically using WKB ray tracing theory and the conservation of wave action.

The synoptic-scale flow, which in the absence of the topography exactly satisfied the nonlinear governing equations, consisted of a barotropic square wave on an f plane superimposed on a uniform westerly current. Over the mountain, the winds were initially calm. As the square wave translated eastward, the cross-mountain winds increased to a maximum halfway through the simulation, and then returned symmetrically to zero. During the period of accelerating cross-mountain flow the momentum flux aloft greatly exceeded that predicted by steady-state theory. No such enhancement was observed during the decelerating phase.

Two factors, wave-packet accumulation aloft and the intensification of the flux within the packets, were responsible for enhancing the momentum fluxes in the accelerating cross-mountain flow. Wave packets accumulated above the mountain because the vertical group velocity of each packet is proportional to the large-scale cross-mountain flow at the time it was launched, and therefore packets launched later in the acceleration phase tended to overtake those launched earlier. The momentum flux carried by each packet intensified to conserve wave action as it propagated through the region where the large-scale velocities increased westward ($\partial U/\partial x < 0$) and its east–west wavelength decreased. Note that this second factor, involving changes in the momentum flux transported by individual packets, is not due simply to flow transience, but rather to horizontal variations in the large-scale velocity field characteristic of any localized barotropic jet.

For almost linear problems the simulated cross-mountain pressure drag generated by a finite three-dimensional ridge in a slowly evolving barotropic flow closely followed that which would be predicted by steady-state linear theory using the instantaneous value of the synoptic-scale cross-mountain wind. Only the momentum flux aloft deviated significantly from the predictions of the steady-state model. For mountains high enough to preserve a moderate degree of nonlinearity when the synoptic-scale cross-mountain flow was strongest (corresponding to minimum values of $Nh/U = 0.25$ or greater), the cross-mountain pressure drag ceased to be symmetric about the time of maximum wind, and the enhancement of the momentum flux aloft during the period of large-scale flow acceleration increased relative to that produced by lower mountains. One consequence of these asymmetries about the time of maximum wind is that the character of the topographically induced disturbance at time t_i could not be determined solely by the local value of the parameter $Nh/U(t_i)$.

Another unanticipated result, obtained both from the simulations and the WKB momentum-flux reconstructions, is that there was a period of about 15 h while the cross-mountain flow was accelerating during which momentum flux convergence developed in the lower troposphere due to the enhanced wave activity aloft, and this convergence temporarily accelerated the domain-averaged low-level flow. In the simulations with a 1-km-high mountain, the vertical momentum flux gradient responsible for this acceleration was even large enough to dominate the effects of wave breaking, so that for a period of several hours, the momentum fluxes above the region of breaking were larger than those below.

One continuing goal of this research is to determine the response of the synoptic-scale flow to the mesoscale perturbations generated by the topography. The mountain-induced response may be revealed by computing difference fields between these simulations and the undisturbed translating square wave, since the latter is an exact nonlinear solution of the governing equations. Details about the dynamical character and spatial structure of the synoptic-scale response, as well as the time- and domain-averaged momentum budgets will be presented in a subsequent paper.

Acknowledgments. The authors are indebted to Dave Muraki and Eric Kunze for helpful discussions. This research was supported by National Science Foundation Grants ATM-0137335, ATM-9980744, and ATM-0228804.

APPENDIX

The WKB Ray Tracing Algorithm

A key assumption in WKB ray tracing is that the wavenumber vector varies slowly in space so that a local phase function may be defined. Following the discussion in Lighthill (1978, p. 310), a physical quantity q in the waves can be expressed in the form of

$$q(x, y, z, t) = Q(x, y, z, t) \exp[i\alpha(x, y, z, t)], \qquad \text{(A1)}$$

where Q is a positive slowly varying amplitude and α is a phase angle. Expanding α around position $\mathbf{x}_0 = (x_0, y_0, z_0)$ at time t_0 yields

$$\alpha(\mathbf{x}_0 + \Delta\mathbf{x}, t_0 + \Delta t) = \alpha(\mathbf{x}_0, t_0) + \Delta x\frac{\partial\alpha}{\partial x} + \Delta y\frac{\partial\alpha}{\partial y} + \Delta z\frac{\partial\alpha}{\partial z} + \Delta t\frac{\partial\alpha}{\partial t} + \frac{\Delta x^2}{2}\frac{\partial^2\alpha}{\partial x^2} + \frac{\Delta y^2}{2}\frac{\partial^2\alpha}{\partial y^2} + \frac{\Delta z^2}{2}\frac{\partial^2\alpha}{\partial z^2} + \frac{\Delta t^2}{2}\frac{\partial^2\alpha}{\partial t^2} + \frac{\Delta x\Delta y}{2}\frac{\partial^2\alpha}{\partial x\partial y} + \frac{\Delta y\Delta z}{2}\frac{\partial^2\alpha}{\partial y\partial z} + \frac{\Delta z\Delta x}{2}\frac{\partial^2\alpha}{\partial z\partial x} + \frac{\Delta y\Delta x}{2}\frac{\partial^2\alpha}{\partial y\partial x} + \frac{\Delta z\Delta y}{2}\frac{\partial^2\alpha}{\partial z\partial y} + \frac{\Delta x\Delta z}{2}\frac{\partial^2\alpha}{\partial x\partial z} + \frac{\Delta x\Delta t}{2}\frac{\partial^2\alpha}{\partial x\partial t} + \frac{\Delta y\Delta t}{2}\frac{\partial^2\alpha}{\partial y\partial t} + \frac{\Delta z\Delta t}{2}\frac{\partial^2\alpha}{\partial z\partial t} + \frac{\Delta t\Delta x}{2}\frac{\partial^2\alpha}{\partial t\partial x} + \frac{\Delta t\Delta y}{2}\frac{\partial^2\alpha}{\partial t\partial y} + \frac{\Delta t\Delta z}{2}\frac{\partial^2\alpha}{\partial t\partial z} + O(\Delta^3), \tag{A2}$$

where all derivatives are evaluated at $(\mathbf{x}_0, t_0)$. WKB theory requires that (A2) is adequately represented by

$$\alpha(\mathbf{x}_0 + \Delta\mathbf{x}, t_0 + \Delta t) \approx \alpha(\mathbf{x}_0, t_0) + \Delta x\frac{\partial\alpha}{\partial x} + \Delta y\frac{\partial\alpha}{\partial y} + \Delta z\frac{\partial\alpha}{\partial z} + \Delta t\frac{\partial\alpha}{\partial t} \tag{A3}$$

for all Δx and Δt within a few wavelengths and wave periods of $(\mathbf{x}_0, t_0)$. Defining

$$\frac{\partial\alpha}{\partial x} = k, \quad \frac{\partial\alpha}{\partial y} = \ell, \quad \frac{\partial\alpha}{\partial z} = m, \quad \frac{\partial\alpha}{\partial t} = -\omega, \tag{A4}$$

consider variations in α that lie along a ray path, in which case

$$\Delta x = c_{gx}\Delta t, \quad \Delta y = c_{gy}\Delta t, \quad \Delta z = c_{gz}\Delta t. \tag{A5}$$

Substituting (A4) and (A5) into (A2), the change in α along a ray path may be written as

$$\alpha(\mathbf{x}_0 + \Delta\mathbf{x}, t_0 + \Delta t) = \alpha(\mathbf{x}_0, t_0) + \Delta x\left(k + \frac{\Delta t}{2}\frac{D_g k}{Dt}\right) + \Delta y\left(\ell + \frac{\Delta t}{2}\frac{D_g \ell}{Dt}\right) + \Delta z\left(m + \frac{\Delta t}{2}\frac{D_g m}{Dt}\right) - \Delta t\left(\omega + \frac{\Delta t}{2}\frac{D_g \omega}{Dt}\right) + O(\Delta^3), \tag{A6}$$

where $D_g/Dt = \partial/\partial t + \mathbf{c}_g \cdot \boldsymbol{\nabla}$ is the material change following the group velocity. For the WKB approximation to hold, the second- and higher-order terms in (A6) must be small compared with the first-order terms. In our calculations, the only significant violations involve rapid variations in α with respect to x. Consequently, our focus is on the second term of the right-hand side of (A6), which should satisfy

$$|k| \gg \left|\frac{\Delta t}{2}\frac{D_g k}{Dt}\right|. \tag{A7}$$

Recalling that $\Delta t = \Delta x/c_{gx}$ along a ray path and requiring (A7) hold for Δx as large as one wavelength, that is, $|\Delta x| \leq 2\pi/k$, (A7) becomes

$$|k|^2 \gg \left|\frac{\pi}{c_{gx}}\frac{D_g k}{Dt}\right| \approx \left|\frac{\pi}{c_{gx}}\frac{\Delta k}{\Delta t}\right| = \pi\left|\frac{\Delta k}{\Delta x}\right|,$$

where Δk is the change in k along the ray over time Δt. Therefore, if the solution to (18) fails to satisfy

$$\left|\frac{\Delta k}{\Delta x}\right| \leq \frac{0.1}{\pi}|k|^2,$$

the variation of k along the ray is limited such that

$$|\Delta k| = \frac{0.1}{\pi}|k|^2|\Delta x|.$$

When the finite ridge is Fourier decomposed on the 1800-km periodic domain, the modes associated with roughly a dozen x-component wavenumbers (k) dominate the momentum flux spectrum. Because there are only a relatively small number of rays associated with modes having these ks, the $z - t$ distribution of the reconstructed momentum flux is rather noisy, with a significant percentage of the flux concentrated along individual ray paths. This noise was eliminated by increasing both the x and y dimensions of the domain by a factor of four, so that near its maximum, the momentum flux was distributed over a more continuous Fourier spectrum. Ray tracing theory was then applied to

all waves in this more continuous spectrum, except that waves for which $2\pi(k^2 + l^2)^{1/2} \geq L/5$ were eliminated because their wavelengths are too long relative to the variations in the synoptic-scale flow to satisfy the WKB approximation.

REFERENCES

Bannon, P. R., and J. A. Zehnder, 1985: Surface pressure and mountain drag for transient airflow over a mountain ridge. *J. Atmos. Sci.,* **42,** 2454–2462.

Bell, T. H., 1975: Lee waves in stratified flows with simple harmonic time dependence. *J. Fluid Mech.,* **67,** 705–722.

Bretherton, F. P., 1969: Momentum transport by gravity waves. *Quart. J. Roy. Meteor. Soc.,* **95,** 213–243.

——, and C. J. Garrett, 1968: Wave trains in inhomogeneous moving media. *Proc. Roy. Soc. London,* **302A,** 529–554.

Crook, N. A., T. L. Clark, and M. W. Moncrieff, 1990: The Denver cyclone. Part I: Generation in low Froude number flow. *J. Atmos. Sci.,* **47,** 2725–2742.

Durran, D. R., 1986: Mountain waves. *Mesoscale Meteorology and Forecasting,* P. S. Ray, Ed., Amer. Meteor. Soc., 472–492.

——, 1999: *Numerical Methods for Wave Equations in Geophysical Fluid Dynamics.* Springer-Verlag, 465 pp.

——, and J. B. Klemp, 1983: A compressible model for the simulation of moist mountain waves. *Mon. Wea. Rev.,* **111,** 2341–2361.

Eliassen, A., and E. Palm, 1960: On the transfer of energy in stationary mountain waves. *Geophys. Publ.,* **22,** 1–23.

Epifanio, C. C., and D. R. Durran, 2001: Three-dimensional effects in high-drag-state flows over long ridges. *J. Atmos. Sci.,* **58,** 1051–1065.

Kim, Y.-J., and A. Arakawa, 1995: Improvement of orographic gravity wave parameterization using a mesoscale gravity wave model. *J. Atmos. Sci.,* **52,** 1875–1902.

Klemp, J. B., and D. K. Lilly, 1978: Numerical simulation of hydrostatic mountain waves. *J. Atmos. Sci.,* **35,** 78–107.

Lighthill, J., 1978: *Waves in Fluids.* Cambridge University Press, 504 pp.

Lilly, D. K., 1962: On the numerical simulation of buoyant convection. *Tellus,* **14,** 148–172.

——, 1972: Wave momentum flux—A GARP problem. *Bull. Amer. Meteor. Soc.,* **53,** 17–23.

——, and J. B. Klemp, 1979: The effects of terrain shape on nonlinear hydrostatic mountain waves. *J. Fluid Mech.,* **95,** 241–261.

Lott, F., and H. Teitelbaum, 1993a: Linear unsteady mountain waves. *Tellus,* **45A,** 201–220.

——, and ——, 1993b: Topographic waves generated by a transient wind. *J. Atmos. Sci.,* **50,** 2607–2624.

McFarlane, N. A., 1987: The effect of orographically excited gravity wave drag on the general circulation of the lower stratosphere and troposphere. *J. Atmos. Sci.,* **44,** 1775–1800.

Nance, L. B., and D. R. Durran, 1997: A modeling study of nonstationary trapped mountain lee waves. Part I: Mean-flow variability. *J. Atmos. Sci.,* **54,** 2275–2291.

Palmer, T. N., G. J. Shutts, and R. Swinbank, 1986: Alleviation of a systematic westerly bias in general circulation and numerical weather prediction models through an orographic gravity-wave drag parameterization. *Quart. J. Roy. Meteor. Soc.,* **112,** 1001–1039.

Peltier, W. R., and T. L. Clark, 1979: The evolution and stability of finite-amplitude mountain waves. Part II: Surface wave drag and severe downslope windstorms. *J. Atmos. Sci.,* **36,** 1498–1529.

Sawyer, J. S., 1959: The introduction of the effects of topography into methods of numerical forecasting. *Quart. J. Roy. Meteor. Soc.,* **85,** 31–43.

Smith, R. B., 1977: The steepening of hydrostatic mountain waves. *J. Atmos. Sci.,* **34,** 1634–1654.

——, 1979: The influence of the mountains on the atmosphere. *Advances in Geophysics,* Vol. 21, Academic Press, 87–230.

Whitham, G. B., 1974: *Linear and Nonlinear Waves.* John Wiley and Sons, 636 pp.